Geophysical Prospecting

EAGE EUROPEAN ASSOCIATION OF GEOSCIENTISTS & ENGINEERS

Geophysical Prospecting, 2013, **61**, 1252–1263 doi: 10.1111/1365-2478.12064

On the role of reflections, refractions and diving waves in full-waveform inversion

V.V. Kazei[1]*, V.N. Troyan[1], B.M. Kashtan[1] and W.A. Mulder[2,3]

[1]*Laboratory of Elastic Media Dynamics, Department of Physics, Saint-Petersburg State University, St. Petersburg, Russia,* [2]*Shell Global Solutions International B.V. PO Box 60, 2280 AB Rijswijk, The Netherlands, and* [3]*Department of Geoscience & Engineering, Faculty of Civil Engineering and Geosciences, Delft University of Technology PO Box 5048, 2600 GA Delft, The Netherlands*

Received October 2012, revision accepted January 2013

ABSTRACT

Full-waveform inversion suffers from local minima, due to a lack of low frequencies in data. A reflector below the zone of interest may, however, help in recovering the long-wavelength components of a velocity perturbation, as demonstrated in a paper by Mora. With the Born approximation for a perturbation in a reference model consisting in two homogeneous isotropic acoustic half-spaces and the assumption of infinitely large apertures available in the data, analytic expressions can be found that describe the spatial spectrum of the recorded seismic signal as a function of the spatial spectrum of the inhomogeneity. Diving waves can be included if the deeper part of the homogeneous model is replaced by one that has a vertical velocity gradient. We study this spectrum in more detail by separately considering scattering of direct, reflected and head waves, as well as singly and multiply reflected diving waves for a gradient model. Taking the reflection coefficient of the deeper reflector into account, we obtain sensitivity estimates for each wavetype. Although the head waves have a relatively small contribution to the reconstruction of the velocity perturbation, compared to the other waves, they contain reliable long-wavelength information that can be beneficial for full-waveform inversion. If the deeper part has a constant positive velocity gradient with depth, all the energy eventually returns to the source-receiver line, given a sufficiently large acquisition aperture. This will improve the sensitivity of the scattered reflected and refracted wavefields to perturbations in the background model. The same happens for a zero velocity gradient but with a very high impedance contrast between the two half-spaces, which results in a large reflection coefficient.

Key words: Full-waveform inversion, Head waves, Sensitivity, Seismic tomography.

1 INTRODUCTION

Full-waveform inversion (FWI) provides more detailed information about physical parameters of the Earth than ray-based methods do but the question still remains whether this information is reliable and which types of waves contribute to the inversion result. A well-known drawback of FWI that leads to erroneous inversion results is the occurrence of local minima in the misfit functional. Bunks *et al.* (1995) showed that the availability of low frequencies in recorded data should improve the smoothness of the misfit functional and reduce the risk of ending up in a local minimum. In practice, the required low frequencies are usually absent from the data but diving-wave tomography (Woodward and Rocca 1988; Pratt *et al.* 1996) can still recover the large-scale structure of the velocity model if the initial velocity model is sufficiently close to the true model.

Mora (1989) wondered if a reflector below the zone of interest would help full-waveform inversion to converge to the proper solution. He assumed a model consisting in two

*E-mail: vkazei@gmail.com

half-spaces with constant velocities and examined the reconstruction of a perturbation in the shallower one. Sources and receivers were located above the perturbation and the reflector and a velocity jump between the half-spaces was located below the perturbation. The perturbation causes scattering of the incoming wavefield from the sources but is also illuminated from below by waves that reflect from the boundary between the two constant-velocity half-space, which are transmitted and forward scattered through the perturbation towards the receivers. In this setting, Mora found that, in principle, FWI should be able to recover the long-wavelength structure of a velocity model by exploiting both the backward and forward scattered waves. The scattered reflected waves improve the illumination of the velocity perturbation and provide long-wavelength information that is absent if only backscattered waves in the shallower half-space are considered. In Mora's analysis, the depth of the reflector below the perturbation need not be known, since it can be reconstructed by migration in the first FWI iteration if the velocity in the top layer is known.

Here, we generalize Mora's model by adding a gradient to the velocity of the deeper layer. Also, we extend his analysis by separately analysing the pure reflections, refracted or head waves (Červený and Ravindra 1971) and diving waves. We then perform a sensitivity analysis to assess the contribution of refracted, reflected and diving waves to the long-wavelength part of the reconstructed velocity perturbation.

Section 2 contains a description of the 2D solution for two homogeneous half-spaces as well as for a homogeneous shallow layer and a deeper layer with a positive, constant velocity gradient. With a reflecting interface between the constant-velocity and gradient layers, the diving waves can propagate down into the gradient layer, return to the interface and be transmitted to the surface or be reflected back into the gradient layer once or several times. We will refer to the latter as 'multiple' diving waves. Traveltime modelling shows that, for a reflecting interface between a shallow constant-velocity layer and a deeper half-space with a velocity gradient, the distinction between the traveltimes of the refracted waves and 'multiple' diving waves is small. Their combined amplitude is much larger than in the case of a homogeneous deeper half-space model, because for an infinite acquisition and infinite recording time, the gradient layer will cause all energy to eventually return to the source-receiver line.

Section 3 describes the inverse problem of estimating a velocity perturbation in a shallow half-space, illuminated by reflected and refracted waves and also by diving waves in case of a deeper gradient model. A sensitivity analysis is presented in section 4, assuming an infinite source and receiver aperture and the main conclusions are summarized in section 5.

2 THE FORWARD PROBLEM

We consider a 2D constant-density acoustic wave equation. The pressure $\hat{p}(\mathbf{r}, t)$ as a function of position $\mathbf{r}$ and time t should obey

$$\frac{1}{v^2}\frac{\partial^2 \hat{p}}{\partial t^2} - \Delta \hat{p} = \hat{f}(\mathbf{r} - \mathbf{r}_0, t), \tag{1}$$

with velocity $v(\mathbf{r})$ and source function $\hat{f}(\mathbf{r} - \mathbf{r}_0, t)$. The assumption of a horizontally layered velocity model, $v(z)$ and Fourier transformations in time and in the horizontal coordinate, x,

$$\hat{p}(\mathbf{r}, t) = \int\int e^{-i\omega t} e^{ik_s x} \tilde{p}(k_x, z, \omega)\, dx\, dt, \tag{2}$$

lead to the 1D Helmholtz equation,

$$\left[-\frac{\omega^2}{v^2(z)} + k_x^2 - \frac{\partial^2}{\partial z^2}\right] \tilde{p}(k_x, z, \omega) = \tilde{f}(k_x, z - z_0, x_0, \omega), \tag{3}$$

with the transformed pressure, $\tilde{p}(k_x, z, \omega)$, depending on the horizontal wavenumber k_x, depth z and angular frequency ω.

In any local domain where the velocity is constant and the source function equals zero, a solution of equation (3) is a linear combination of two exponentials, $\exp(\pm i z\sqrt{(\omega/v)^2 - k_x^2})$, corresponding to upgoing and downgoing wavefields. We need this representation of the wavefield to obtain results in a closed form for the inverse problem in section 3. Also, the velocity in the region where we want to invert for a perturbation in the velocity model should be locally constant. Outside this region, the velocity may vary. Examples of suitable background velocity profiles are shown in Fig. 1.

Wolf (1937) was the first geophysicist to derive and analyse the reflection coefficient for model no. 4, a transition layer in which the velocity varies linearly with depth but only for plane waves at normal incidence. For model no. 5 and plane waves at oblique incidence, the problem was solved analytically by Gupta (1965). More general results for this problem and for model no. 6 can be found in the work of Wadhwa (1971), including an analytical asymptotic solution for a point source. Unfortunately, the analytical expressions for the reflection coefficients are so complicated that the analysis, still continuing today (Liner and Bodmann 2010), is often restricted to normal incidence.

To obtain a better understanding of FWI while having closed-form expression, we have to consider oblique angles of incidence. For the inversion result, we also need a velocity

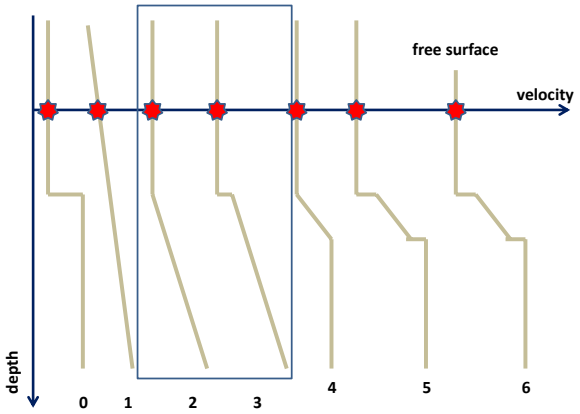

Figure 1 A set of velocity background models that can be of interest for analysing full-waveform inversion.

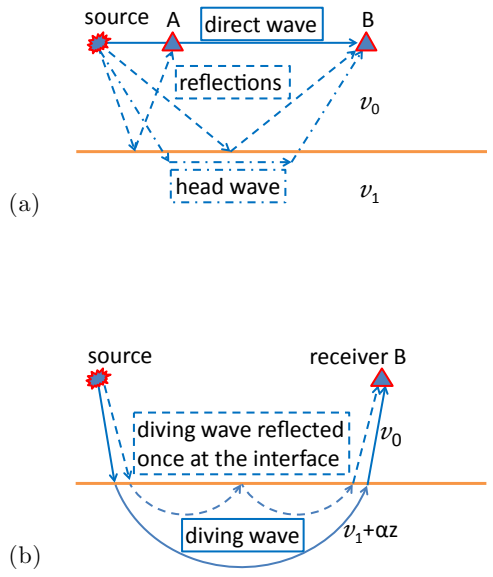

Figure 2 (a) Wavepaths from a source to a receiver in a model with two acoustic half-spaces. The shallower half-space, where the source and receiver are located, has a constant velocity v_0 and the deeper half-space a velocity v_1. Direct waves (solid lines) and reflected waves (dashed lines) occur for all offsets. The reflection from the source to receiver B is called overcritical or total reflection. Head waves (dash-dotted lines) are present for angles of incidence beyond the critical angle. (b) Additional wavepaths from the source to receiver occur when the deeper half-space has a linear velocity profile of the form $v_1 + \alpha z$, with $\alpha > 0$. The shallower half-space still has a velocity v_0. Standard diving waves (solid lines) appear together with 'multiple' diving waves (dashed lines), reflected once or several times from the interface. The wavetypes in (a) are present as well but have not been drawn. Note that the 'multiple' diving waves start to resemble head waves when the number of reflections tends to infinity.

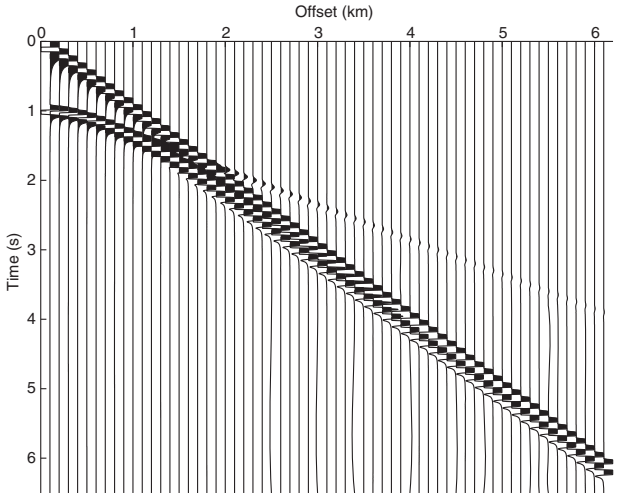

Figure 3 Head waves for two homogeneous half-spaces, with velocities of 1 km/s in the shallow and 2 km/s in the deeper part and an interface at 500-m depth, have their amplitudes decaying with offset. The direct wave is strongly clipped.

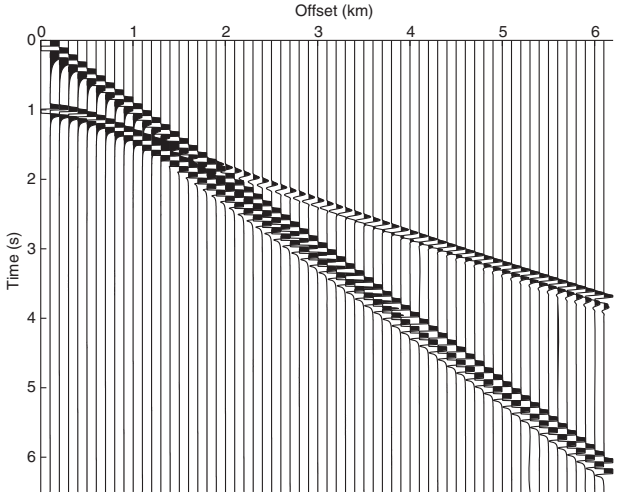

Figure 4 The superposition of head waves and diving waves, when the deeper medium has a velocity gradient of 0.5 s^{-1}, has amplitudes increasing with offset.

perturbation located in the homogeneous part of the model. For this reason, we discard model no. 1, which has been studied elsewhere (Pekeris 1946; Kuvshinov and Mulder 2006; Mulder and Plessix 2008). We only will consider the nos. 0 and 3 as background velocity models, with 2 as the limiting case of 3 and avoid the more complex models 4–6.

Figure 2 depicts the various types of waves that occur in model nos. 0 and 3. The seismograms are displayed in Figs 3

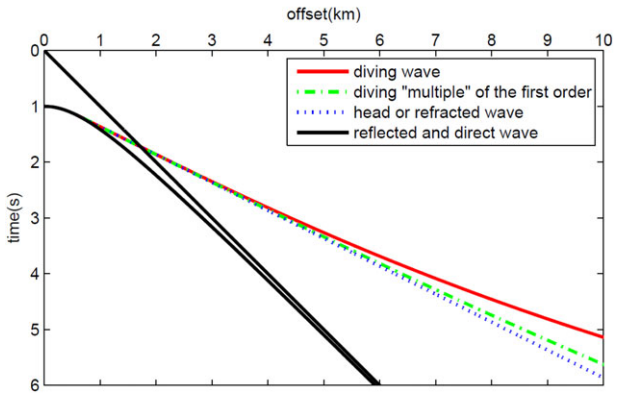

Figure 5 Traveltime curves for direct and reflected waves (black), a diving wave (red), head wave (blue) and a wave that has been reflected once at the interface between the shallower and deeper half-space (green).

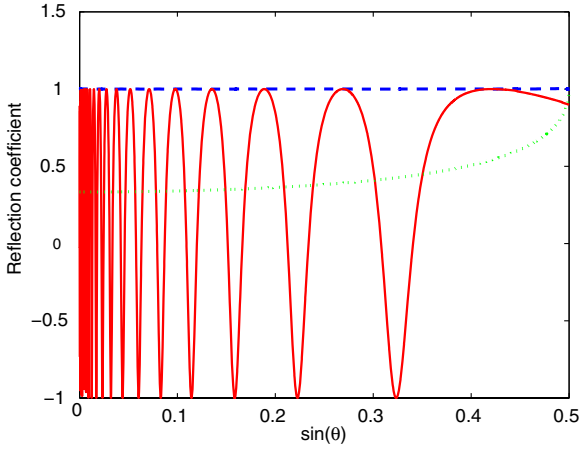

Figure 6 Reflection coefficient for oblique incidence at an angle θ in the case of two homogeneous half-spaces with $v_1/v_0 = 2$ (green dotted). For a model with a gradient in the deeper half-space with $v_0 = 1$ km/s, $v_1 = 2$ km/s and a gradient $\alpha = 0.5\,\mathrm{s}^{-1}$ at an angular frequency $\omega = 5$ Hz, the absolute value (blue dashed) and real part (red solid) of the reflection coefficient are shown.

and 4, respectively. The first example consists in two half-spaces, separated by an interface at a depth $z_1 = 500$ m and velocities $v_0 = 1$ km/s in the shallow and $v_1 = 2$ km/s in the deeper part. For the second example, the shallow velocity is the same but the deeper layer has a velocity of the form $v(z) = v_1 + \alpha(z - z_1)$, with $\alpha = 0.5\,\mathrm{s}^{-1}$. Comparing the seismograms in Figs 3 and 4, it is evident that the diving waves and 'multiple' diving waves cannot be distinguished by time gating from the head waves for the current, high contrast between the shallow and deeper layers. At lower contrasts and larger gradients, diving waves can be separated by their traveltimes but head waves are still mixed with the higher-order 'multiple' diving waves.

The velocity gradient in the deeper layer causes more wave energy to return back to the receivers and boosts the amplitudes of the apparent 'head' waves, which are a combination of true head waves and diving waves from the deeper layer. Figure 5 shows the traveltimes for head waves, normal diving waves and a diving 'multiple' of first-order as well as reflected waves for the same example of model no. 3 as in Figure 4. The traveltime for the diving wave is derived in Appendix A. For not too large offsets, the traveltimes almost coincide and the diving waves boost the amplitude of the combined waves. We will examine this in more detail next by considering the reflection coefficient for model nos. 0 and 3.

Reflection coefficients

The solution of the forward problem for two homogeneous half-spaces with a point source can be found in, for instance, Brekhovskikh and Godin (1999). In the next section, which will cover the inverse problem of recovering an inhomogeneity in a shallow homogeneous layer, we only need the reflection coefficient for the two homogeneous half-spaces as well as for the problem with a gradient layer in the deeper part.

After a Fourier transformation in time and in the horizontal coordinates, the incident wavefield is

$$\tilde{p}_0 = \exp(iz\sqrt{k_0^2 - k_x^2}), \quad k_0 = \omega/v_0, \tag{4}$$

and the reflected one is

$$\tilde{p}_1 = C(k_x)\exp(-iz\sqrt{k_0^2 - k_x^2}). \tag{5}$$

In the case of two homogeneous half-spaces, $\alpha = 0$, the reflection coefficient is (Brekhovskikh and Godin 1998, p. 21)

$$C(k_x) = \frac{1-b}{1+b}, \quad b = \frac{\sqrt{\frac{\omega^2}{v_1^2} - k_x^2}}{\sqrt{k_0^2 - k_x^2}}. \tag{6}$$

This coefficient is real and has an absolute value increasing with the angle of incidence up to the critical angle; see the green curve in Fig. 6. At the critical angle, total reflection starts to occur and beyond the critical angle, head waves appear.

We can express the reflection coefficient into a term corresponding head waves and to pure reflections:

$$C = C_{\mathrm{head}} + C_{\mathrm{refl}} = -\frac{2b}{1-b^2} + \frac{1+b^2}{1-b^2}. \tag{7}$$

The first term inherits standard branch points from the full coefficient. Its integration along the branch cuts in the complex plane near the branch points yields the usual head waves (Brekhovskikh and Godin 1999, p. 11). The square-roots have been removed from the second term that now describes the pure reflections, without the head waves. We use the split in equation (7) only at overcritical angles, where b is purely imaginary. The coefficients then satisfy the energy relation $|C|^2 = |C_{\text{head}}|^2 + |C_{\text{refl}}|^2$, with purely imaginary C_{head} and real-valued C_{refl}. This separation will enable us to estimate the individual contributions of these two wavetypes later on.

For a positive gradient in the deeper half-space, the velocity is $v(z) = v_1 + \alpha(z - z_1)$ with $\alpha > 0$ and the diving waves in the gradient layer obey (Kuvshinov and Mulder 2006)

$$\tilde{p}_2 = W(k_x)\sqrt{\tilde{z}}\ K_\nu(k_x\tilde{z}), \quad \tilde{z} = z - z_1 + v_1/\alpha, \tag{8}$$

where $\nu = i\sqrt{(\omega/\alpha)^2 - 1/4}$. K_ν is the Macdonald or modified Bessel function of the second kind and $W(k_x)$ is the amplitude. Continuity of pressure and displacement at the interface implies $\tilde{p}_0 + \tilde{p}_1 = \tilde{p}_2$ and $\partial(\tilde{p}_0 + \tilde{p}_1)/\partial z = \partial\tilde{p}_2/\partial z$ at $z = z_1$, leading to the reflection and transmission coefficients

$$C(k_x) = \frac{1-b}{1+b}, \quad W(k_x) = \frac{2}{(1+b)\sqrt{v_1/\alpha}\ K_\nu(\xi)}, \tag{9}$$

with

$$b = \frac{\alpha}{iv_1\sqrt{k_0^2 - k_x^2}}\left(\frac{1}{2} + \frac{\xi K_\nu'(\xi)}{K_\nu(\xi)}\right), \tag{10}$$

$$= \frac{\alpha}{iv_1\sqrt{k_0^2 - k_x^2}}\left(\frac{1}{2} + \nu - \frac{\xi K_{\nu+1}(\xi)}{K_\nu(\xi)}\right) \tag{11}$$

and $\xi = k_x v_1/\alpha$. The modified Bessel function $K_\nu(x)$ for a purely imaginary order ν is real for any $x > 0$ and its derivative with respect to x is also real (Dunster 1990). Therefore, the denominator in equation (9) equals the numerator's complex conjugate if $|k_x| < |k_0|$, as can be seen from equation (10), implying that $|C(k_x)| = 1$.

Figure 6 shows graphs of the reflection coefficient for the two model nos. 0 and 3. The reflection angle θ follows from $\sin\theta = k_x/k_0$. The contribution to the absolute value of the wavefield amplitude from the diving waves is defined by the difference between the blue dashed curve and the green dotted curve. For $|k_x| > |k_0|$, the waves decay exponentially with distance from the deeper half-space and will therefore not be considered.

3 INVERSION

The aim of our work is to investigate the effect of head and diving waves on the inversion result. The Born approximation (Bleistein, Cohen and Stockwell 2001) is used for the scattered field δu as a function of frequency for a point source at x_s and receiver at x_r and at the same depth $z_s = z_r$:

$$\delta u(x_s, x_g) = f_\omega \int k_0^2 G(x_s, \mathbf{r})\delta W(\mathbf{r}) G(x_g, \mathbf{r}) d\mathbf{r}. \tag{12}$$

Here, $\delta W(\mathbf{r}) = \frac{\delta(1/v^2(\mathbf{r}))}{1/v^2(\mathbf{r})} \simeq \frac{-2\delta v}{v}$ is a small, relative perturbation of the background squared slowness. The Green's functions from the source or receiver to the point $\mathbf{r}$ are $G(x_s, \mathbf{r})$ and $G(x_g, \mathbf{r})$, respectively. We assume the wavelet f_ω at frequency ω to be the same for all sources. Since we will only consider a single frequency later on, we drop this factor. After Fourier transformations in the horizontal coordinates of sources and receivers, the wavefield perturbation is given by

$$\delta\tilde{u}(k_s, k_g) = \int k_0^2 \delta\widetilde{W}(\mathbf{r})\tilde{G}(k_s, \mathbf{r})\tilde{G}(k_g, \mathbf{r}) d\mathbf{r}. \tag{13}$$

Now, $\tilde{G}$ is the Green's function for the background medium in spectral space, or a Fourier transform of the standard frequency-domain Green's function, G. Appendix A provides explicit expressions for $\tilde{G}$ in the background models 0 and 3. Using the analytical expression for the Green's function of the background medium provided in Appendix B, a linear relation between the full-wavefield perturbation spatial spectrum and the inhomogeneity spatial spectrum is obtained:

$$\begin{aligned}\delta\tilde{u}(k_s, k_g) \sim\ & \delta\widetilde{W}(\mathbf{s}_+ + \mathbf{g}_+) + C(k_g)\delta\widetilde{W}(\mathbf{s}_+ + \mathbf{g}_-) \\ & + C(k_s)\delta\widetilde{W}(\mathbf{s}_- + \mathbf{g}_+) + C(k_s)C(k_g)\delta\widetilde{W}(\mathbf{s}_- + \mathbf{g}_-).\end{aligned} \tag{14}$$

Here $\delta\widetilde{W}(\mathbf{K}) = \int \delta W(\mathbf{r}) e^{i(\mathbf{K}\cdot\mathbf{r})} d\mathbf{r}$ is a typical 2D Fourier transform of the squared slowness perturbation, where $\mathbf{K} = (K_x, K_z)^T$ is a vector in the spatial Fourier domain. $C(k_s)$ and $C(k_g)$ are the reflection coefficients for the respective monochromatic plane waves from the boundary between the half-spaces. The first term corresponds to the combination of waves that go directly from the source to the perturbation and from the perturbation to a geophone. Its inverse represents migration in a homogeneous background. Similarly, inversion of the second and third term corresponds to reflection tomography and the fourth term to migration of scattered waves coming from the deeper reflector (Mora 1989). The details of the derivation for formula (14) can be found in Appendix B, resulting in equation (B7). The vectors are defined as

$$\mathbf{s}_\pm = \begin{pmatrix} k_s \\ \mp\gamma_s \end{pmatrix}, \qquad \mathbf{g}_\pm = \begin{pmatrix} k_g \\ \mp\gamma_g \end{pmatrix}, \tag{15}$$

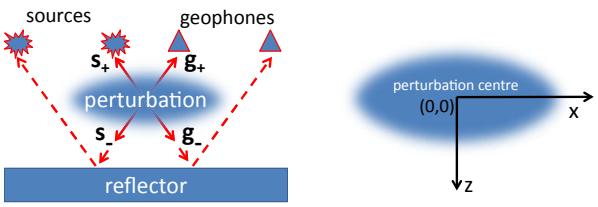

(a) (b)

Figure 7 (a) Source and receiver wavepaths through the centre of the scatterer, described by the vectors $\mathbf{s}_\pm$ and $\mathbf{g}_\pm$. (b) The system of coordinates in which we perform spatial Fourier transformations of data and perturbation.

and the roots are $\gamma_s = \sqrt{k_0^2 - k_s^2}$ and $\gamma_g = \sqrt{k_0^2 - k_g^2}$ with $k_0 = \omega/v_0$. Both are positive in the domain of interest by definition. We should mention that, due to the downward direction of the z-axis, the positive direction in the Fourier space is downwards, so when, for instance, $\mathbf{s}_+$ and $\mathbf{g}_+$ point upwards, they have negative vertical components. Figure 7 shows typical directions of source and receiver wavepaths passing through the centre of the inhomogeneity.

Equation (14) depends linearly on the spatial Fourier transform of the squared slowness perturbation. We should emphasize that this special linear dependence holds for wavefields in a homogeneous medium, enabling a straight-forward decomposition into monochromatic plane waves. If a perturbation is placed in a region with a varying velocity, the simple relation between the spectrum of the perturbation and the wavefields is lost.

We are able to construct points $\mathbf{K}_i$ in the inhomogeneity spectrum that have an influence on the spectral amplitude for each point (k_s, k_g) in the wavefield spectrum, according to equation (14). These points are defined by

$$\mathbf{K}_1 = \mathbf{s}_+ + \mathbf{g}_+, \quad \mathbf{K}_4 = \mathbf{s}_- + \mathbf{g}_-, \tag{16}$$

$$\mathbf{K}_2 = \mathbf{s}_+ + \mathbf{g}_-, \quad \mathbf{K}_3 = \mathbf{s}_- + \mathbf{g}_+. \tag{17}$$

Formula (16) defines the component of the perturbation that can be recovered by migration, whereas equation (17) contains components recoverable by tomography based on reflected waves. Although there are four points in the perturbation spectrum related to one in the wavefield spectrum, the inverse transformation is unique. For the computations in the next section 4, we need to know the inverse transformation, meaning we should express (k_s, k_g) in terms of $\mathbf{K} = (K_x, K_z)^{\mathrm{T}}$. Because the right-hand side of equation (14) is symmetric in the pairs (k_s, k_g) and (k_g, k_s), we do not have to distinguish between them. In Appendix B, we prove that there is a unique pair (k_s, k_g) for each $\mathbf{K}$, up to transposition of k_s and k_g.

Equation (14) will be used in the next section to calculate the perturbation of the full wavefields in models 0 and 3 as well as the perturbations of the wavefields that correspond to the reflections $\delta\tilde{u}_{\mathrm{refl}}$ and refractions or head waves $\delta\tilde{u}_{\mathrm{head}}$, as defined in equation (7). For the head waves, we have

$$\delta\tilde{u}_{head}(k_s, k_g) \sim C_{head}(k_g)\delta\widetilde{W}(\mathbf{K}_2) + C_{head}(k_s)\delta\widetilde{W}(\mathbf{K}_3) + C_{head}(k_s)C_{head}(k_g)\delta\widetilde{W}(\mathbf{K}_4). \tag{18}$$

The right-hand side of equation (18) contains the scattered field of the reflector, assuming that the perturbation is located at some distance from the reflector and that the latter only produces head waves and no pure reflections (we refer to Appendix C for details). This could be the case if one would try to only invert for the earlier arrivals (Sheng *et al.* 2006), excluding the later reflections and direct waves. For equation (18) and the similar expression (19) for $\delta\tilde{u}_{\mathrm{refl}}(k_s, k_g)$ with only the reflections, we have

$$\delta\tilde{u}_{\mathrm{refl}}(k_s, k_g) \sim C_{\mathrm{refl}}(k_g)\delta\widetilde{W}(\mathbf{K}_2) + C_{\mathrm{refl}}(k_s)\delta\widetilde{W}(\mathbf{K}_3) + C_{\mathrm{refl}}(k_s)C_{\mathrm{refl}}(k_g)\delta\widetilde{W}(\mathbf{K}_4). \tag{19}$$

Some of the cross terms of $C(k_s)C(k_g)$, namely $C_{\mathrm{head}}(k_s)C_{\mathrm{refl}}(k_g)$ and $C_{\mathrm{refl}}(k_s)C_{\mathrm{head}}(k_g)$, were neglected. They have neither the high propagation velocities of refractions nor the large amplitudes of reflections, so they only have a small contribution to the inversion result. The cross terms were, however, retained in the expression for the full-wavefield perturbation.

4 SPECTRAL SENSITIVITIES

The relation between the wavefield perturbation spatial spectrum and the inhomogeneity spatial spectrum is presented in the form of sensitivity diagrams. For the perturbation of the full wavefield, the sensitivity is defined as

$$S_{\mathrm{full}}(\mathbf{K}) = \left| \frac{\partial\delta\tilde{u}(k_s(\mathbf{K}), k_g(\mathbf{K}))}{\partial\delta\widetilde{W}(\mathbf{K})} \right|, \tag{20}$$

where $\mathbf{K}$ equals one of the $\mathbf{K}_i$, $i = 1, \ldots, 4$. If we only consider the head waves, we obtain

$$S_{\mathrm{head}} = \left| \frac{\partial\delta\tilde{u}_{\mathrm{head}}(k_s(\mathbf{K}), k_g(\mathbf{K}))}{\partial\delta\widetilde{W}(\mathbf{K})} \right|. \tag{21}$$

Because the diagrams depend linearly on the frequency through $\mathbf{K} \propto k_0$ with $k_0 = \omega/v_0$, we only have to consider a single frequency. Figure 8 shows diagrams of the sensitivity

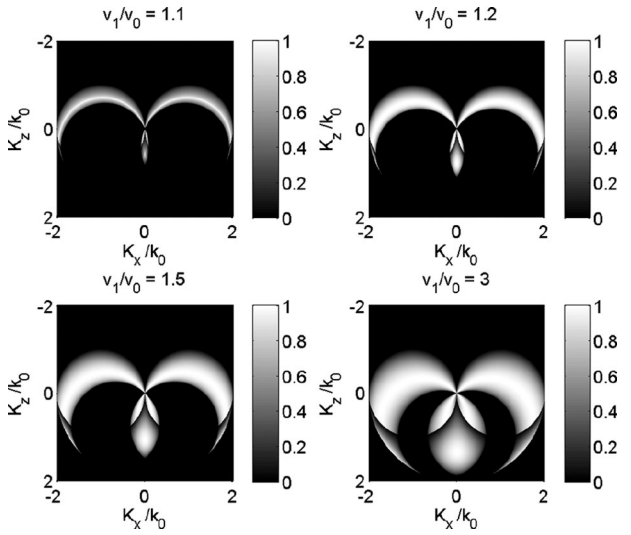

Figure 8 Sensitivity diagrams for head waves coming from the deeper half-space and scattered by the perturbation, for various velocity contrasts.

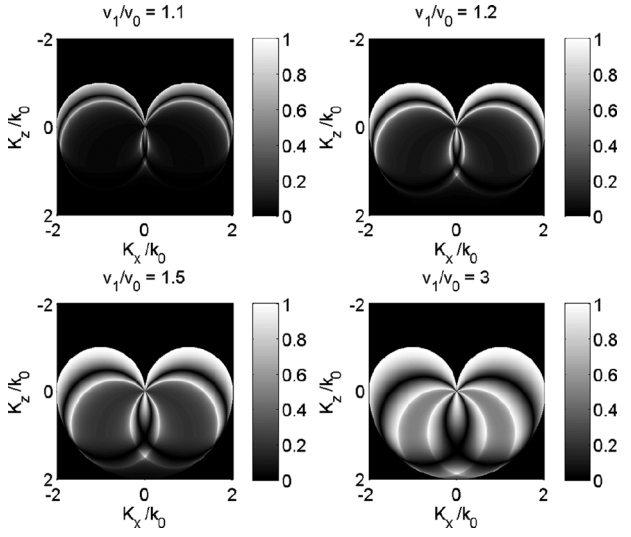

Figure 9 As Fig. 8 but for reflected waves.

of the head waves to the perturbations in the inhomogeneity spectrum for three different velocity contrasts of the background model, using equation (21). For comparison, Fig. 9 corresponds to the sensitivity of pure reflections, given by

$$S_{\text{refl}} = \left| \frac{\partial \delta \tilde{u}_{\text{refl}}(k_s(\mathbf{K}), k_g(\mathbf{K}))}{\partial \delta \widetilde{W}(\mathbf{K})} \right|. \tag{22}$$

Fig. 10 displays diagrams for the sensitivity of the full wavefield spectrum for the same parameters, using equation (20). Fig. 11 illustrates the behaviour of the sensitivity at very high and very low velocity contrasts in the case of two constant-

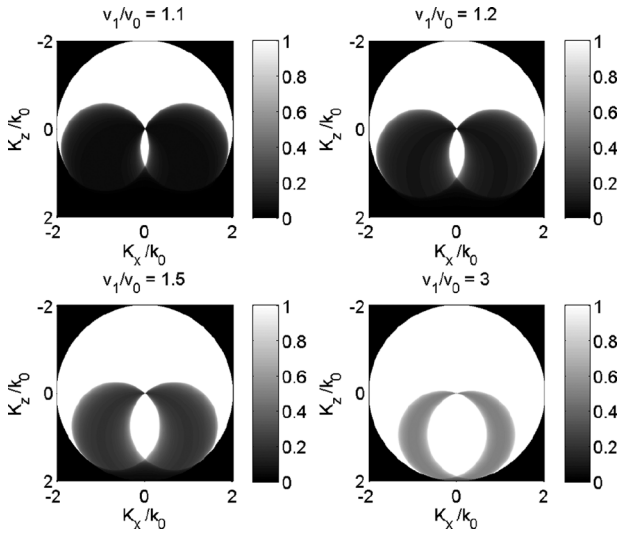

Figure 10 As Fig. 8 but for the full wavefield.

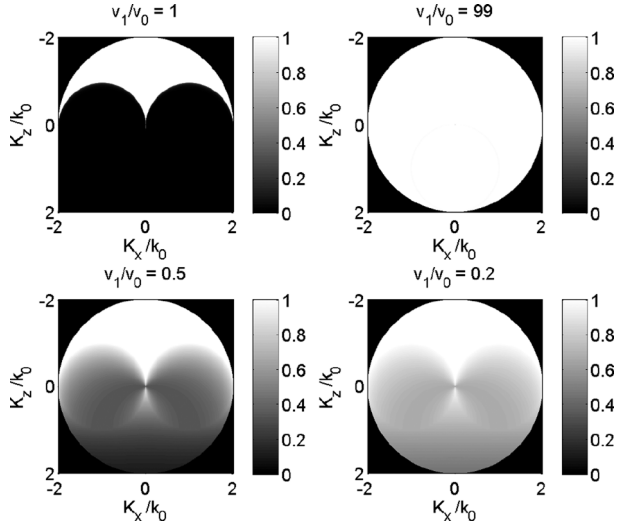

Figure 11 Spectral sensitivities of the full wavefield to variations in the perturbation's spatial spectrum. The top-right panel shows that the sensitivity approaches 1 inside the circle of radius 2 for high velocity contrasts ($v_1/v_0 \gg 1$ or $v_0/v_1 \gg 1$). The bottom row shows sensitivities for intermediate contrasts when $v_1 < v_0$.

velocity half-spaces, with the constant-velocity case as a reference in the left-upper panel. This last picture shows the part of spectrum that can be recovered if there is no reflector at all and that can be reconstructed by migration in a homogeneous background. The top-right panel of Fig. 11 together with Fig. 10 shows that the sensitivity approaches unity in the circle of radius 2 if the half-space has a much higher velocity than the shallow one. In this case, nearly all energy is reflected. The low-sensitivity part has an area that is determined by the

critical angle of incidence, which becomes smaller when the velocity in the deeper half-space increases relative to the velocity in the shallower part. For the bottom row of Fig. 11, the deeper half-space has a lower velocity than the shallow one. There are no head waves and the shape of the region with low sensitivity does not depend on the contrast between the layers. However, contrary to case $v_1/v_0 > 1$, neither the shape nor the area of the low-sensitivity region depend on the contrast between the layers, since there is no critical angle in this case. The low sensitivity increases to a high sensitivity of one when the velocity ratio v_1/v_0 decreases to zero, because nearly all energy is reflected at the interface. In either case, $v_1/v_0 > 1$ or $v_1/v_0 < 1$, the illumination becomes uniform at a very high contrast as the reflection coefficient has an amplitude close to 1 for all angles of incidence.

For the model with a positive velocity gradient in the deeper layer, the absolute value of the reflection coefficient is always equal to one. It then follows from equations (14) and (20) that the sensitivity, S_3, of the full wavefield in model no. 3 equals one:

$$S_3 = 1 = S_{\text{full}} + S_{\text{diving}}. \tag{23}$$

Details can be found in Appendix B. Equation (23) defines S_{diving} as the sensitivity of the wavefield that was not available in model no. 0 and that can be attributed to the diving waves: $S_{\text{diving}} = S_3 - S_{\text{full}} = 1 - S_{\text{full}}$. As a result, the diving waves will result in a sensitivity equal to 1 inside the circle of radius 2, similar to the right-upper diagram of Fig. 11. This will enable the recovery of the spatial perturbation spectrum that had a low sensitivity in Fig. 10. However, the area of this low-sensitivity part of the perturbation spectrum is determined by the critical angle of incidence at which the absolute value of the reflection coefficient becomes one. Its area decreases when the velocity in the deeper half-space increases ($v_1 > v_0$).

As the white regions correspond to maximum sensitivity, the bright arcs in Fig. 8 mark the part of the spectrum that can be more reliably recovered by head waves than by reflections. As it turns out, these domains are rather small. However, despite their small size, they are important because these domains cannot be reconstructed from pure reflections, as illustrated by the diagrams in Fig. 9. They contain the low-vertical wavenumbers of the perturbation, which are important for velocity model updating with FWI. Also, from the series of diagrams in Figs 8 and 9, we conclude that the lower the velocity contrast, the higher is the importance of head waves for improving the sensitivity to all wavenumbers of the perturbation. Even at high contrasts, some of the low-vertical wavenumbers in the perturbation spectrum are better retrieved by head waves than by pure reflections.

5 CONCLUSIONS

We analysed the contributions of head waves, pure reflections and diving waves in two half-spaces, the shallow one with a constant velocity and the deeper one with a constant zero or positive velocity gradient in depth, to the recovery of the spatial spectrum of a velocity inhomogeneity when using full-waveform inversion. In the case of two constant-velocity half-spaces, spatial vertical wavenumbers of a perturbation restored by the head waves are lower than those for reflections. Therefore, head waves can help full-waveform inversion to reconstruct the long-wavelength structure of the velocity model.

It also became apparent that the sensitivity of the full wavefield does not depend on the parameters of the half-spaces if the deeper one has a positive gradient. The amplitudes of the 'head waves' are significantly boosted by 'multiple' diving waves, to the advantage of full-waveform inversion in such models. In this case and with an infinite range of sources and receivers, all energy will eventually return to the receivers and the perturbation will be uniformly illuminated from all directions. The lower the velocity contrast of the deeper reflector, the larger is the relative contribution of diving waves compared to pure reflections and head waves. The same behaviour occurs for two constant-velocity half-spaces with a unit reflection coefficient or infinite impedance contrast. The lower the contrast at the interface between the half-spaces, the larger is the contribution of the diving waves, assuming the aperture of the acquisition is sufficiently large. Finally, we note that acquisition effects were ignored and that their impact needs to be investigated.

ACKNOWLEDGEMENTS

The authors express their gratitude to Fons ten Kroode of Shell Global Solutions International B.V. for proposing and supporting this project as well as to Jean Virieux and Marwan Charara for stimulating discussions during the EAGE 2012 annual meeting in Copenhagen. The authors are also grateful for the remarks and suggestions of the reviewers.

REFERENCES

Bleistein N., Cohen J. and Stockwell J. 2001. *Mathematics of Multi-dimensional Seismic Imaging, Migration, and Inversion. Interdisciplinary Applied Mathematics.* Springer. ISBN 9780387950617.

Brekhovskikh L.M. and Godin O.A. 1998. *Acoustics of Layered Media I: Plane and Quasi-Plane Waves. Wave Phenomena*. Springer. ISBN 9783540647249.

Brekhovskikh L.M. and Godin O.A. 1999. *Acoustics of Layered Media II: Point Sources and Bounded Beams. Wave Phenomena*. Springer. ISBN 9783540655923.

Bunks C., Saleck F.M., Zaleski S. and Chavent G. 1995. Multiscale seismic waveform inversion. *Geophysics* **60**(5), 1457–1473.

Červený V. 2001. *Seismic Ray Theory*. Cambridge University Press. ISBN 0521366712.

Červený V. and Ravindra R. 1971. *Theory of Seismic Head Waves*. University of Toronto Press.

Devaney A.J. 1984. Geophysical diffraction tomography. *IEEE Transactions on Geoscience and Remote Sensing* **GE-22**(1), 3–13.

Dunster T. 1990. Bessel functions of purely imaginary order, with an application to second-order linear differential equations having a large parameter. *SIAM Journal on Mathematical Analysis* **21**(4), 995–1018.

Gupta R.N. 1965. Reflection of plane waves from a linear transition layer in liquid media. *Geophysics* **30**(1), 122–132.

Kuvshinov B.N. and Mulder W.A. 2006. The exact solution of the time-harmonic wave equation for a linear velocity profile. *Geophysical Journal International* **167**(2), 659–662.

Liner C.L. and Bodmann B.G. 2010. The Wolf ramp: Reflection characteristics of a transition layer. *Geophysics* **75**(5), A31–A35.

Mora P. 1989. Inversion = migration + tomography. *Geophysics* **54**(12), 1575–1586.

Mulder W.A. and Plessix R. 2008. Exploring some issues in acoustic full-waveform inversion. *Geophysical Prospecting* **56**(6), 827–841.

Pekeris C.L. 1946. Theory of propagation of sound in a half-space of variable sound velocity under conditions of formation of a shadow zone. *The Journal of the Acoustical Society of America* **18**(2), 295–315.

Pratt R.G., Song Z.M., Williamson P.R. and Warner M.R. 1996. Two-dimensional velocity models from wide-angle seismic data by waveform inversion. *Geophysical Journal International* **124**(2), 323–340.

Sheng J., Leeds A., Buddensiek M. and Schuster G.T. 2006. Early arrival waveform tomography on near-surface refraction data. *Geophysics* **71**(4), U47–U57.

Wadhwa S.K. 1971. Reflected and refracted waves from a linear transition layer. *Pure and Applied Geophysics* **89**, 45–66.

Wolf A. 1937. The reflection of elastic waves from transition layers of variable velocity. *Geophysics* **2**(4), 357–363.

Woodward M.J. and Rocca F. 1988. Wave-equation tomography. *SEG Technical Program Expanded Abstracts* **7**(1), 1232–1235.

Wu R. and Toksöz M. 1987. Diffraction tomography and multisource holography applied to seismic imaging. *Geophysics* **52**(1), 11–25.

APPENDIX A

DERIVATION OF DIVING WAVES TRAVELTIMES

We derive the traveltime for a ray passing through a homogeneous half-space and a medium with a linear velocity gradient,

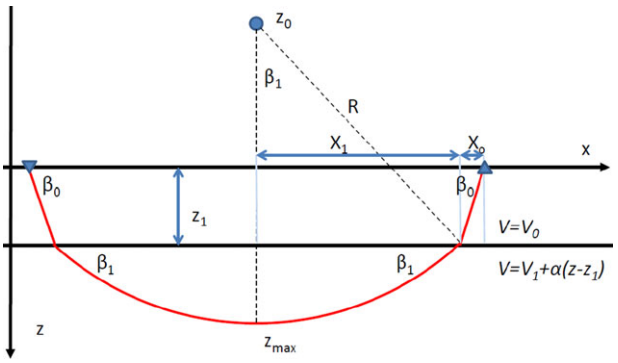

Figure A1 The raypath of a diving wave in a velocity gradient is an arc of the circle with its centre at the point z_0 where the velocity should be zero if it had the same gradient everywhere.

as sketched in Fig. A1. In the domain with the gradient, the ray becomes a diving wave and returns back to the surface. The derivation of the traveltimes for diving waves in the case of a constant velocity gradient without a homogeneous overburden can be found in the book of Červený (2001, p. 167–169). In this medium, the rays are circles with their centres located on the line where the velocity is zero. If $v(z) = v_1 + \alpha(z - z_1)$, this happens at a depth $z_0 = z_1 - v_1/\alpha$. The radius R of the circle is $R = z_{\max} - z_0 = z_{\max} - z_1 + v_1/\alpha$, with $z_{\max}$ the maximum depth reached by the ray. Let h be the offset, the distance between the source and receiver and T the traveltime of a ray connecting the two. Then $h = 2(h_0 + h_1)$, as can be seen in the figure, and $T = 2(T_0 + T_1)$, with T_0 the time spent by the ray on the straight line between the source and the interface, or, by symmetry, the interface and the receiver. The time spent on the circle between the interface and the largest depth is T_1. For derivations, it is easier to express $h(R)$ and $T(R)$ as a function of the radius R.

From the definition of $z_0 = z_1 - v_1/\alpha$ and the geometric relation $z_1 - z_0 = R\cos\beta_1$, it follows that

$$R\cos\beta_1 = v_1/\alpha, \tag{A1}$$

With Snell's law, $v_0^{-1}\cos\beta_0 = v_1^{-1}\cos\beta_1$, this leads to $\cos\beta_0 = v_1/(\alpha R)$. Then,

$$h_0 = z_1\frac{\cos\beta_0}{\sin\beta_0} = z_1\frac{\frac{v_0}{\alpha R}}{\sqrt{1-\left(\frac{v_0}{\alpha R}\right)^2}} \tag{A2}$$

and the traveltime in the shallower constant-velocity layer becomes

$$T_0 = \frac{z_1}{v_0\cos\beta_0} = \frac{z_1}{v_0\sqrt{1-\left(\frac{v_0}{\alpha R}\right)^2}}. \tag{A3}$$

The geometric relation $h_1 = R\sin\beta_1$ together with equation (A1) provides

$$h_1 = R\sin\beta_1 = \sqrt{R^2 - \left(\frac{v_1}{\alpha}\right)^2}. \tag{A4}$$

Integration over the circle's arc produces T_1:

$$T_1 = \int_0^{\beta_1} \frac{R}{V(\beta)}\, d\beta = \frac{1}{\alpha}\text{arccosh}(\alpha R/v_1). \tag{A5}$$

Finally, we obtain

$$h = \frac{2h}{\sqrt{(\alpha R/v_0)^2 - 1}} + 2\frac{v_1}{\alpha}\sqrt{(\alpha R/v_1)^2 - 1} \tag{A6}$$

and

$$T = \frac{2h\alpha R}{v_0^2\sqrt{(\alpha R/v_0)^2 - 1}} + \frac{2}{\alpha}\text{arccosh}(\alpha R/v_1). \tag{A7}$$

Figure A1 shows a single diving wave, the arc in the deeper part. If there is a velocity contrast, $v_1 \neq v_0$, part of the energy will be transmitted into the shallower layer and part will be reflected back, starting a new arc of the same shape. The corresponding traveltimes or these multiply reflected diving waves are easily obtained by multiplying h_1 and T_1 by the number of arcs in the deeper half-space.

The traveltimes of the diving wave, head wave and single reflections are drawn in Fig. 5. It is obvious that for not too large offsets the traveltimes are almost identical and it is impossible to distinguish them at low frequencies.

APPENDIX B

SPATIAL SPECTRA OF A PERTURBATION AND WAVEFIELD

Devaney (1984), Mora (1989) and Wu and Toksöz (1987) derived the relation between the wavenumber spectra of a perturbation and its scattered field. We will first review their work and then extend it to our case.

We start with the Born approximation for the wavefield scattered by a perturbation of the background velocity model. If we consider a source, indexed by s, and a receiver, labelled by g, at the same fixed depth, $z_s = z_g$, then the Born approximation for the wavefield scattered by a perturbation defined by $\delta W(\mathbf{r}) = \frac{\delta(1/v^2(\mathbf{r}))}{1/v^2(\mathbf{r})}$ for a source at x_s and a receiver at x_g provides

$$\delta u(x_s, x_g) = \int k_0^2 \delta W(\mathbf{r}) G(\mathbf{r}_s;\mathbf{r}) G(\mathbf{r}_g;\mathbf{r}) d\mathbf{r}, \tag{B1}$$

where $k_0 = \omega/v_0$. $G(x_s, \mathbf{r})$ is the 2D Green's function for the background medium with a source at $\mathbf{r}$ and receiver at $(x_s, z_{s,g})$ in the frequency domain.

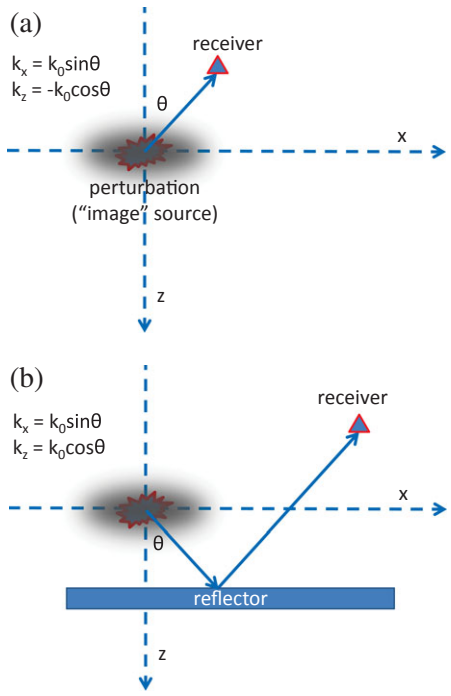

Figure B1 (a) Backscattering of the direct wave produces an upgoing wave in the direction of $\mathbf{g}_+$ towards the receiver. The scatterer acts as an 'image' source (Mora 1989). (b) With a reflector, forward scattering of the direct wave can be viewed as an 'image' source that produces a downgoing wave in the direction $\mathbf{g}_-$, which reaches the receiver after reflection.

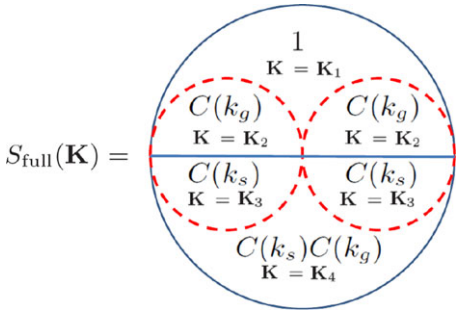

Figure B2 The four regions inside the big circle correspond to four different combinations of signs in equation (B10). These are defined by $\mathbf{K}_1 = \mathbf{s}_+ + \mathbf{g}_+$, $K_z = -\gamma_s - \gamma_g$ for 1; $\mathbf{K}_2 = \mathbf{s}_+ + \mathbf{g}_-$, $K_z = -\gamma_s + \gamma_g$ for $C(k_g)$; $\mathbf{K}_3 = \mathbf{s}_- + \mathbf{g}_+$, $K_z = +\gamma_s - \gamma_g$ for $C(k_s)$; $\mathbf{K}_4 = \mathbf{s}_- + \mathbf{g}_-$, $K_z = +\gamma_s + \gamma_g$ for $C(k_s)C(k_g)$. We have assumed that $|k_s| \leq |k_g|$.

We next perform a Fourier transformation in x_s and x_g of the form

$$\tilde{u}(k_s, k_g) = \int\int e^{i(k_s x_s + k_g x_g)} u(x_s, x_g) dx_s dx_g. \tag{B2}$$

Using the fact that

$$\int e^{ik_s x_s} G(\mathbf{r}_s;\mathbf{r})dx_s = e^{ik_s x}\int e^{ik_s(x_s-x)}G(|\mathbf{r}_s-\mathbf{r}|)dx_s = e^{ik_s x}\tilde{G}(k_s,\mathbf{r}), \tag{B3}$$

where $\tilde{G}(k_s,\mathbf{r})$ is a solution of the 1D Helmholtz equation (3), the Born approximation becomes

$$\delta\tilde{u}(k_s,k_g) = \int k_0^2\,\delta W(\mathbf{r})\tilde{G}(k_s,\mathbf{r})\tilde{G}(k_g,\mathbf{r})d\mathbf{r}. \tag{B4}$$

For a simple background model with receivers and sources placed in its homogeneous part, we obtain the following explicit expression (Mora 1989):

$$\tilde{G}(k_s,\mathbf{r}) = \frac{i}{2}\frac{e^{i\gamma_s d_+}}{\gamma_s}e^{i\mathbf{s}_+\cdot\mathbf{r}} + C(k_s)\frac{i}{2}\frac{e^{i\gamma_s d_-}}{\gamma_s}e^{i\mathbf{s}_-\cdot\mathbf{r}}, \tag{B5}$$

with

$$C(k_s) = \frac{1-b}{1+b},\quad b = \frac{\sqrt{\frac{\omega^2}{v_1^2}-k_s^2}}{\sqrt{k_0^2-k_s^2}},\quad \gamma_s = \sqrt{k_0^2-k_s^2}. \tag{B6}$$

Here, $d_+ = z_{s,g} - z_c$ is the vertical distance between the source-receiver line and the centre of the perturbation region or the approximate vertical distance travelled by the direct ray from the perturbation to the source-receiver line; see Fig. B1(a). Likewise, $d_- = z_1 - z_c + z_{s,g} - z_c$ is the distance travelled by a reflected ray from the perturbation centre to the source-receiver line; see Fig. B1(b).

If the background medium is homogeneous, the Green function is well-known. This is the first term in equation (B5). The second term is related to all the waves that are coming from the interface between the two half-spaces.

Replacing the Green's functions in equation (B4) with their analytical expressions, we arrive at

$$\begin{aligned}\delta\tilde{u}(k_s,k_g) = -\frac{k_0^2\,\tilde{f}_\omega(k_s)}{4\gamma_s\gamma_g}\Bigg(&D_{(++)}\int \delta W(\mathbf{r})e^{i(\mathbf{s}_+ + \mathbf{g}_+)\cdot\mathbf{r}}d\mathbf{r}\\ &+ D_{(+-)}C(k_g)\int \delta W(\mathbf{r})e^{i(\mathbf{s}_+ + \mathbf{g}_-)\cdot\mathbf{r}}d\mathbf{r}\\ &+ D_{(-+)}C(k_s)\int \delta W(\mathbf{r})e^{i(\mathbf{s}_- + \mathbf{g}_+)\cdot\mathbf{r}}d\mathbf{r}\\ &+ D_{(--)}C(k_s)C(k_g)\int \delta W(\mathbf{r})e^{i(\mathbf{s}_- + \mathbf{g}_-)\cdot\mathbf{r}}d\mathbf{r}\Bigg).\end{aligned} \tag{B7}$$

The $D_{(\pm\pm)}$ coefficients represent phase shifts along the wavepaths from the source-receiver line to the expected depth of the inhomogeneity:

$$\begin{aligned}D_{(++)} &= e^{i\gamma_s d_+ + i\gamma_g d_+},\quad D_{(--)} = e^{i\gamma_s d_- + i\gamma_g d_-},\\ D_{(+-)} &= e^{i\gamma_s d_+ + i\gamma_g d_-},\quad D_{(-+)} = e^{i\gamma_s d_- + i\gamma_g d_+}.\end{aligned} \tag{B8}$$

Since their absolute values are equal to one, they will disappear from the sensitivity as explained later on. Also, the factor $-k_0^2\,\tilde{f}_\omega(k_s)/(4\gamma_s\gamma_g)$ was dropped, because it only contains effects related to the source.

We next present the procedure that allows us to obtain explicit relations between points in the data spectrum, $\delta\tilde{u}(k_s,k_g)$, and points in the spatial spectrum, $\delta\widetilde{W}(K_x,K_z)$, of the perturbation. In principle, this relation is defined by equations (14) and (15). Here, we provide more details. The arguments of the function $\delta\widetilde{W}$ in equation (14) are precisely the points of the spatial spectrum of the perturbation related to (k_s,k_g). There are four of them, according to equations (16) and (17). When we try to invert this relation to find $(k_s(\mathbf{K}),k_g(\mathbf{K}))$, we should assume that at least one of the four equations (16), (17) is satisfied. All these equations have the same projection on the x-axis,

$$k_s + k_g = K_x, \tag{B9}$$

which should be satisfied whichever equation of the four is satisfied. For the z-axis, there are four different projections, which can be expressed by means of the integers m and n as

$$(-1)^m\gamma_s + (-1)^n\gamma_g = K_z,\quad m,n\in\{1,2\}. \tag{B10}$$

Recall that $\gamma_{s,g} = \sqrt{k_0^2-k_{s,g}^2}$. We can solve for k_s and k_g from the expressions to obtain

$$k_s = \frac{K_x}{2} \pm \frac{K_z}{2}\sqrt{\frac{4k_0^2}{K_x^2+K_z^2}-1}, \tag{B11}$$

$$k_g = \frac{K_x}{2} \mp \frac{K_z}{2}\sqrt{\frac{4k_0^2}{K_x^2+K_z^2}-1}. \tag{B12}$$

Note that this implies that $K_x^2 + K_z^2 \le (2k_0)^2$. These formulas define k_s and k_g up to their transposition, meaning that they can be interchanged without changing the right-hand side of equation (14). To obtain uniqueness, we impose $|k_s| \le |k_g|$. The signs defined by the integers m and n can be determined by finding the correct combination from equation (B10). The four cases mentioned in equations (16) and (17) and the related sign choices defined by m and n are drawn in Fig. B2. In this way, the computation of the sensitivity $|\partial(\delta\tilde{u})/\partial(\delta\widetilde{W})|$ is reduced to finding the reflection coefficients for various k_s and k_g. For each choice of (K_x,K_z), only one region is involved and therefore only one term of the expression for $\delta\tilde{u}$ in equation (B7). Taking the absolute value then removes any dependence on the $D_{(\pm\pm)}$ coefficients in equation (B8).

If the absolute value of both reflection coefficients equals one, then we obtain a sensitivity equal to 1 everywhere. This

happens in the case of a positive gradient in the deeper half-space, which causes all energy to eventually return to the receiver line.

APPENDIX C

DECOMPOSITION OF THE SCATTERED WAVEFIELD

Born approximation (13) provides the perturbation of the whole wavefield. Here, we split this perturbation into head waves and reflected waves using equation (7). If there were no pure reflections, the wavefield for a point source in the background medium could be found in the same way as in Appendix B:

$$\tilde{G}_{\text{noRefl}}(k_s, \mathbf{r}) = \frac{i}{2}\frac{e^{i\gamma_s d_+}}{\gamma_s} e^{i\mathbf{s}_+\cdot\mathbf{r}} \quad + C_{\text{head}}(k_s)\frac{i}{2}\frac{e^{i\gamma_s d_-}}{\gamma_s} e^{i\mathbf{s}_-\cdot\mathbf{r}}. \tag{C1}$$

Using this Green's function in Born approximation (B4), we obtain

$$\delta\tilde{u}_{\text{noRefl}}(k_s, k_g) = \int k_0^2 \delta W(\mathbf{r}) \tilde{G}_{\text{noRefl}}(k_s, \mathbf{r}) \tilde{G}_{\text{noRefl}}(k_g, \mathbf{r}) d\mathbf{r} \tag{C2}$$

and arrive at an expression similar to equation (14):

$$\begin{aligned}\delta\tilde{u}_{\text{noRefl}}(k_s, k_g) &\sim \delta\widetilde{W}(\mathbf{s}_+ + \mathbf{g}_+) \\ &+ C_{\text{head}}(k_s)\delta\widetilde{W}(\mathbf{s}_+ + \mathbf{g}_-) + C_{\text{head}}(k_g)\delta\widetilde{W}(\mathbf{s}_- + \mathbf{g}_+) \\ &+ C_{\text{head}}(k_s)C_{\text{head}}(k_g)\delta\widetilde{W}(\mathbf{s}_- + \mathbf{g}_-).\end{aligned} \tag{C3}$$

The first term is the result of the direct wavefield being backscattered by the perturbation in the upper half-space. The remaining three terms are due to scattering by the same perturbation of the head waves generated by the deeper reflector. The second term describes wave from the source that were refracted and then scattered before arriving at the receiver. The third term captures waves that started at the source, were then scattered, refracted and returned to the receiver. The last term, the smallest, represents head waves scattered into head waves by the perturbation. This justifies equation (18). Similar arguments lead to equation (19).

Finally, we would like to point out that in the wavenumber representation, the notion of head waves propagating horizontally (in the lower half-space) or in a direction defined by the critical angle (in the upper half-space) is not apparent, since we use a decomposition into harmonic plane waves. The contribution of the head waves in this decomposition is given by

$$u_{\text{head}}(x_s, \mathbf{r}) = \int C_{\text{head}}(k_s)\frac{i}{2}\frac{e^{i\gamma_s d_-}}{\gamma_s} e^{i\mathbf{s}_-\cdot\mathbf{r}} e^{-ik_s x_s} dk_s. \tag{C4}$$

The integral involves a range of wavenumbers k_s that have non-zero $C_{\text{head}}(k_s)$. As a result, neither $\mathbf{s}_\pm$ nor $\mathbf{g}_\pm$ are fixed, although Figs 2 and 7 may suggest otherwise.